

## Fission fragment mass yields and total kinetic energy release in neutron-induced fission of $^{233}\text{U}$ from thermal energies to 40 MeV

D. Higgins <sup>1,2,\*</sup> U. Greife,<sup>1</sup> F. Tovesson,<sup>2</sup> B. Manning,<sup>2</sup> D. Mayorov <sup>2</sup> S. Mosby,<sup>2</sup> and K. Schmitt<sup>2</sup>

<sup>1</sup>Colorado School of Mines, Physics Department, 1500 Illinois St., Golden, Colorado 80401, USA

<sup>2</sup>Los Alamos National Laboratory, PO Box 1663, Los Alamos, New Mexico 87545, USA



(Received 5 July 2019; revised manuscript received 22 September 2019; published 3 January 2020)

Properties of fission in  $^{233}\text{U}$  were measured at the Los Alamos Neutron Science Center at incident neutron energies from thermal to 40 MeV. Fragments were observed in coincidence by using a twin ionization chamber with Frisch grids. The average total kinetic energy released and fragment mass yields were determined by using the double energy analysis method based on conservation of mass and momentum. The experimental method was validated by using  $^{232}\text{Th}$  and absolute energy was calibrated by using thermal-neutron-induced fission of  $^{235}\text{U}$ . This work incorporates novel applications of multi-chance fission channel cross sections and fission models to account for the complexities introduced by prompt neutron emission at high energy and extends results up to higher incident neutron energies than previously measured. Accurate experimental measurements of these parameters are necessary to better understand the fission process in isotopes central to the thorium fuel cycle.

DOI: [10.1103/PhysRevC.101.014601](https://doi.org/10.1103/PhysRevC.101.014601)

### I. INTRODUCTION

The majority of energy released in neutron-induced fission of actinides is in the form of kinetic energy in the fission fragments. The average total kinetic energy (TKE) released has been shown to have a dependency on the incident neutron energy  $E_n$  and has been well characterized for several isotopes at thermal  $E_n$ . However, this dependency is inadequately understood and there have been few measurements at fast energies [1]. Since future reactor designs are expected to generate harder neutron spectra, these data in the fast regime are needed. The white neutron source at the Los Alamos Neutron Science Center (LANSCE) can provide these measurements and this work is part of an ongoing experimental campaign conducted at LANSCE to obtain average TKE on relevant actinides. The detector used was an ionization chamber with twin back-to-back volumes and Frisch grids. Correlated measurements of fragment energy were used to calculate the fragment mass distributions based on conservation of mass and momentum using the double energy ( $2E$ ) analysis method [2]. This work presents measurements of the average TKE and fragment mass yields of  $^{233}\text{U}$  and characterizes how these parameters change with  $E_n$  from thermal to 40 MeV. The measurement and analysis method used in this experiment for both total kinetic energy and fragment mass distribution was validated by using  $^{232}\text{Th}$ , which is a much better characterized isotope. Accurate experimental measurements of these parameters serve as valuable inputs for modeling nuclear systems necessary for the development of future nuclear reactor designs.

### II. EXPERIMENT

#### A. Facility

This experiment was conducted at LANSCE, a linear accelerator at the Los Alamos National Laboratory capable of producing up to 800 MeV protons. Two facilities were used to take measurements, the Weapons Neutron Research (WNR) facility and the Lujan Neutron Scattering Center. At the WNR the high-energy proton beam is directed onto an unmoderated tungsten spallation source which generates neutrons from 200 keV to  $>600$  MeV [3]. Both the  $^{233}\text{U}$  and  $^{232}\text{Th}$  targets were measured in the 90L WNR flight path with an 11.9 m flight path length. The pulsed timing structure of the beam consisted of a series of 125 ps micropulses spaced 1.8  $\mu\text{s}$  apart and grouped into 675  $\mu\text{s}$  macropulses delivered at 40 Hz. Fission from low-energy neutrons was measured at flight path 12 of the Lujan Center with a 22 m flight path length. Protons are delivered to the Lujan Center via the 1L target area using water and liquid hydrogen moderators to generate thermal and sub-thermal neutrons at a 20 Hz repetition rate.

#### B. Experimental setup

A synopsis of the experimental set up used in this work is provided here and a more detailed description is given in Refs. [4,5]. This experiment was conducted by using a steel-bodied cylindrical ionization chamber with two back-to-back detection volumes positioned on-axis along the neutron beamline. Each volume had a circular anode with a Frisch grid and a shared cathode between the two. The cathode also supported the sample target material, which was positioned at the center of the cathode normal to the beamline. Both samples were supported on a thin  $100 \pm 10 \mu\text{g}/\text{cm}^2$  carbon foil backing which was itself secured to the cathode by a thin aluminum ring. The Th sample consisted of a full circle deposit of

\*dhiggins@alumni.mines.edu

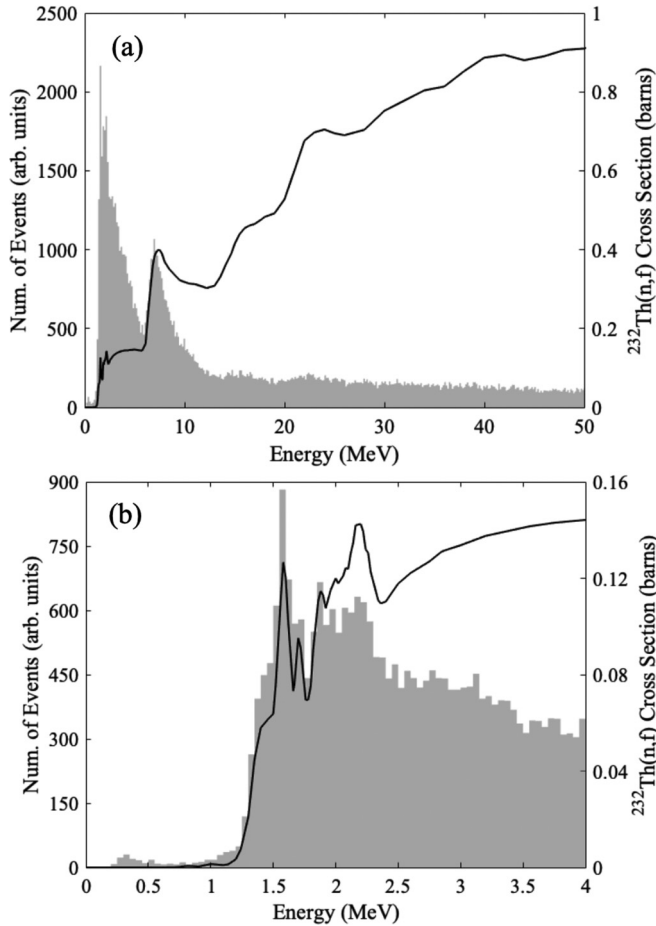


FIG. 1. (a) The  $E_n$  spectrum, shown in the shaded region, is compared with the neutron-induced fission cross section for  $^{232}\text{Th}$  [7]. (b) A close-up view at lower energy shows a good correlation between features in both the  $E_n$  spectrum and the cross section. There is an overall trend in decreased counts at higher energy due to the increased neutron flux at lower energy.

603.6  $\mu\text{g}$  of isotopically pure  $^{232}\text{Th}$  with an area density of 192.1  $\mu\text{g}/\text{cm}^2$ . The  $^{233}\text{U}$  sample, enriched to  $> 99\%$  was also a full circle deposit that contained 226.1  $\mu\text{g}$  of U with an area density of 72  $\mu\text{g}/\text{cm}^2$ . Constant current density molecular plating was used to deposit this sample. The plating solvent used in this process, an isopropanol-isobutanol mixture, has been shown to result in a residual layer of cracked solvent molecules on the surface of the target referred to as crud [6]. Energy loss of fission fragments traveling through the solvent layer was corrected for using the same method as that used to correct for fragment energy loss in the backing and target material itself which is discussed further in Sec. III B. The ionization chamber used P-10 fill gas (90% Ar, 10%  $\text{CH}_4$ ); the anodes were biased to 1000 V, and the cathode to  $-1500$  V.

The accelerator delivered a pulse signal when the proton beam reached the tungsten spallation target which served as the start signal for the neutron time-of-flight measurement. The signal from the cathode was used as the stop time for the neutron time of flight. The two anode signals were used to determine the energy of the ionizing particle in the gas and

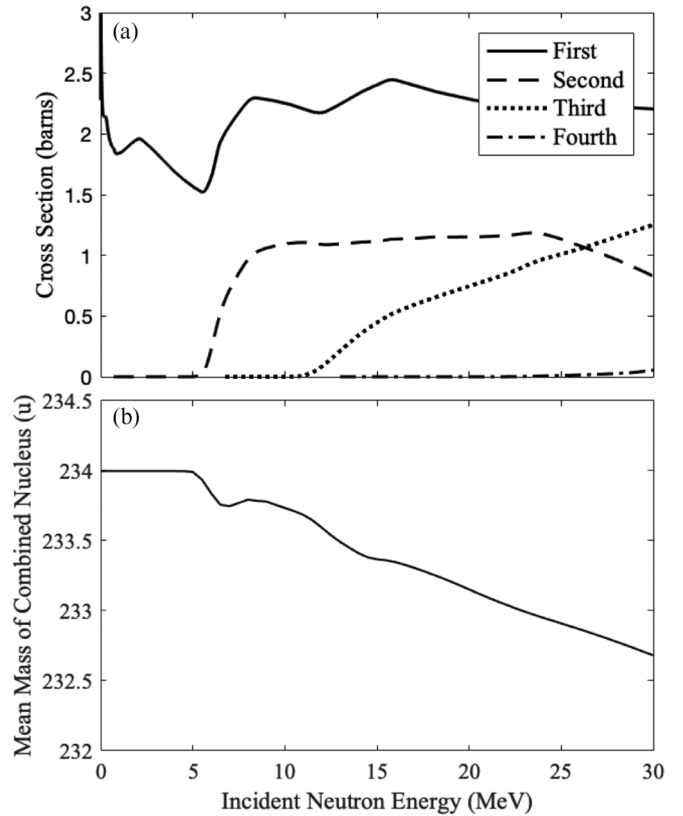


FIG. 2. (a) Cross sections for first-, second-, third-, and fourth-chance fission in  $^{233}\text{U}$  [7]. The proportional probability of various fission chances varies continuously, which is used in this work to determine the mean mass of the combined nucleus prior to scission, shown in panel (b).

the two signals from the Frisch grids were used to determine the angle of emission of each particle.

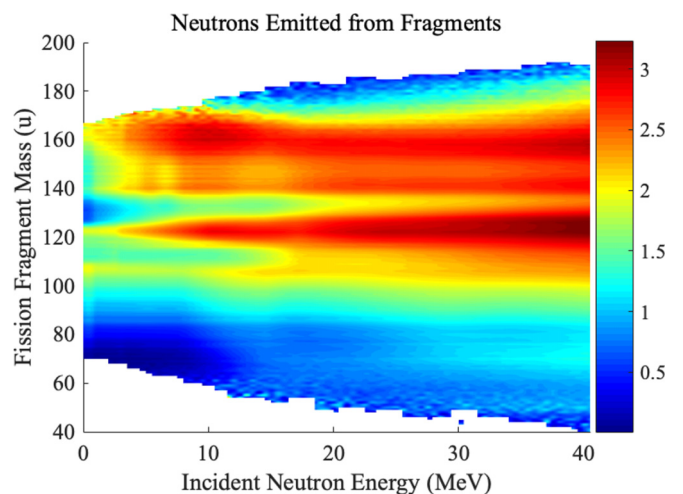


FIG. 3. Neutron emission from  $^{233}\text{U}(n, f)$  after scission was dependent on both the fission fragment mass and the incident neutron energy.

### III. ANALYSIS

#### A. Neutron energy

The neutron energy is calculated by using the time-of-flight method. For data collected from the  $^{232}\text{Th}$  sample, a few apparent features can be identified in the uncalibrated time-of-flight spectrum. A small sharp peak at very early arrival time, referred to as the photofission peak, was caused by gamma-induced fission from photons released from the spallation target. It is useful for calibrating the neutron time-of-flight spectrum since the photons that caused these events have a known speed. The timing resolution of the detector was determined by fitting the photofission peak to a Gaussian curve, the full-width at half-maximum of which gave a resolution of 1.3 ns.

Certain features in the time-of-flight spectrum, consisting of sharp changes in counts, were correlated with resonance features in the  $^{232}\text{Th}(n, f)$  cross section with known energies at 1.58, 1.70, and 6.10 MeV, which are used to identify the neutron energy at which those events occurred. These, along with the photofission peak, were used to determine the flight path length to high precision and calibrate the time-of-flight spectrum to energy as shown in Fig. 1.

A second method was used to calibrate the  $^{233}\text{U}$  measurements using a carbon block placed in the beamline upstream from the detector. A distinct feature in the  $^{12}\text{C}$  neutron scattering cross section at 2.078 MeV results in a sharp drop in measured fission events at that energy. This feature, again along with the photofission peak, were used to calibrate to neutron energy. The two methods used for calibration were in strong agreement with each other, well within the timing resolution of the detector.

#### B. Fragment energy

Determining the energy of the fission fragments was done by analyzing the anode pulse heights as well as calculating fragment angle of emission from the grid signals. The anode pulse heights from the two volumes showed a bimodal distribution with a narrow feature at high energy and a broader feature at low energy. The narrow feature was generated by light fragments since they carry away a greater share of kinetic energy [8]. The angle of emission was needed in order to apply corrections to the anode pulse height spectra to account for differences between the two volumes. These differences included energy loss of the fragments traveling through the target backing and the cracked solvent layer, momentum transfer of the incident neutron, and gain differences between the preamps. This method is described in greater detail in Refs. [2,5].

Once these corrections were calculated and applied, the anode pulse height spectra of the two volumes overlapped one another, indicating that all differences between the two volumes had been properly accounted for. The two features of the bimodal anode spectra were fit to Gaussian distributions, the means of which were taken as the light and heavy fragments from which a linear fit was made to calibrate to energy based on the dominant fragment masses and energies [9–11].

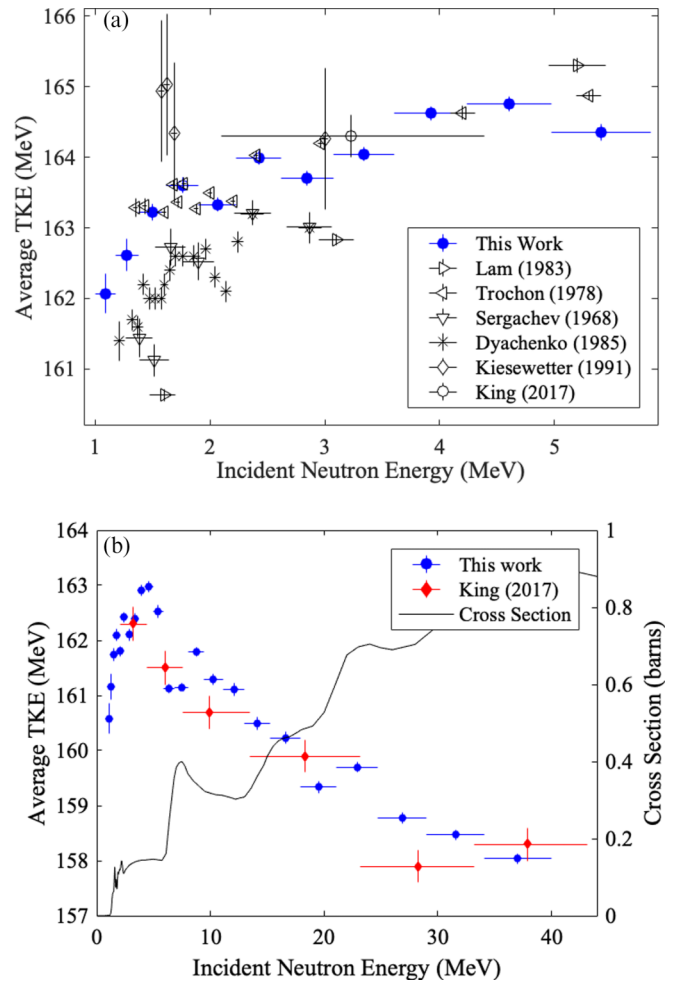


FIG. 4. (a) Average TKE in  $^{232}\text{Th}(n, f)$  results from this work show good agreement with several past results at low energy [9,11,13–16]. (b) Comparison at high energy also shows good agreement shown here up to 40 MeV for post-neutron emission along with the neutron-induced fission cross section [7,17]. Vertical error bars show statistical uncertainty; horizontal error bars correspond to neutron energy bins.

#### C. Prompt neutron emission

The mass and energy of the fission fragments were found by using a calculation based on conservation of mass and momentum that iteratively adjusts the masses and corrects for mass-dependent variations such as the pulse height defect until the mass of the fission fragments converge to within a threshold. It is dependent on having the correct mass of the system, both before and after scission. The mass of the combined nucleus is based on the mass of the target nucleus plus the mass of the incident neutron. However, this value can vary with  $E_n$  due to the onset of second and higher chance fission reactions in which neutron emission occurs prior to scission [8]. The probability of these reactions increases with increasing  $E_n$ , which is reflected in the cross section for multi-chance fission as shown for  $^{233}\text{U}$  in Fig. 2. The mean mass of the combined nucleus prior to scission depends directly on the

TABLE I. Average TKE and standard deviation for neutron-induced fission of  $^{233}\text{U}$  both before and after neutron emission.

$E_n$ (MeV)	Pre-neutron emission		Post-neutron emission	
	Avg. TKE (MeV)	$\sigma_{\text{TKE}}$ (MeV)	Avg. TKE (MeV)	$\sigma_{\text{TKE}}$ (MeV)
0.12 ± 0.12	170.13 ± 0.004	13.33 ± 0.003	168.24 ± 0.004	13.13 ± 0.003
0.25 ± 0.02	170.16 ± 0.05	13.42 ± 0.04	168.25 ± 0.05	13.22 ± 0.03
0.29 ± 0.02	170.07 ± 0.05	13.51 ± 0.03	168.16 ± 0.05	13.31 ± 0.03
0.34 ± 0.03	170.18 ± 0.04	13.46 ± 0.03	168.26 ± 0.04	13.26 ± 0.03
0.40 ± 0.03	170.22 ± 0.04	13.49 ± 0.03	168.30 ± 0.04	13.29 ± 0.03
0.47 ± 0.04	170.15 ± 0.04	13.47 ± 0.03	168.23 ± 0.04	13.27 ± 0.03
0.55 ± 0.04	170.15 ± 0.04	13.45 ± 0.02	168.23 ± 0.03	13.24 ± 0.02
0.64 ± 0.05	170.19 ± 0.03	13.36 ± 0.02	168.27 ± 0.03	13.15 ± 0.02
0.75 ± 0.06	170.16 ± 0.03	13.42 ± 0.02	168.24 ± 0.03	13.21 ± 0.02
0.87 ± 0.07	170.14 ± 0.03	13.39 ± 0.02	168.22 ± 0.03	13.18 ± 0.02
1.02 ± 0.08	170.11 ± 0.03	13.35 ± 0.02	168.20 ± 0.03	13.15 ± 0.02
1.19 ± 0.09	170.14 ± 0.03	13.42 ± 0.02	168.22 ± 0.03	13.21 ± 0.02
1.40 ± 0.11	170.09 ± 0.03	13.36 ± 0.02	168.17 ± 0.03	13.15 ± 0.02
1.63 ± 0.13	170.06 ± 0.03	13.43 ± 0.02	168.12 ± 0.03	13.22 ± 0.02
1.91 ± 0.15	170.13 ± 0.03	13.42 ± 0.02	168.13 ± 0.03	13.21 ± 0.02
2.23 ± 0.17	170.11 ± 0.03	13.45 ± 0.02	168.09 ± 0.03	13.23 ± 0.02
2.61 ± 0.20	170.00 ± 0.03	13.49 ± 0.02	167.95 ± 0.03	13.27 ± 0.02
3.05 ± 0.24	170.02 ± 0.03	13.51 ± 0.02	167.93 ± 0.03	13.28 ± 0.02
3.56 ± 0.28	169.91 ± 0.03	13.53 ± 0.02	167.78 ± 0.03	13.30 ± 0.02
4.16 ± 0.32	169.90 ± 0.03	13.62 ± 0.02	167.74 ± 0.03	13.40 ± 0.02
4.87 ± 0.38	169.67 ± 0.03	13.55 ± 0.02	167.46 ± 0.03	13.32 ± 0.02
5.69 ± 0.44	169.47 ± 0.04	13.74 ± 0.03	167.23 ± 0.04	13.51 ± 0.03
6.66 ± 0.52	169.25 ± 0.03	13.57 ± 0.02	167.01 ± 0.03	13.34 ± 0.02
7.78 ± 0.61	169.10 ± 0.04	13.66 ± 0.02	166.77 ± 0.03	13.43 ± 0.02
9.10 ± 0.71	168.84 ± 0.04	13.79 ± 0.03	166.36 ± 0.04	13.56 ± 0.03
10.63 ± 0.83	168.72 ± 0.04	13.87 ± 0.03	166.10 ± 0.04	13.63 ± 0.03
12.43 ± 0.97	168.07 ± 0.05	13.95 ± 0.03	165.37 ± 0.05	13.71 ± 0.03
14.53 ± 1.13	167.70 ± 0.05	14.00 ± 0.03	164.94 ± 0.05	13.77 ± 0.03
16.99 ± 1.32	167.61 ± 0.05	13.93 ± 0.04	164.81 ± 0.05	13.70 ± 0.04
19.86 ± 1.55	166.85 ± 0.06	14.23 ± 0.04	163.91 ± 0.05	13.99 ± 0.04
23.22 ± 1.81	166.96 ± 0.06	14.34 ± 0.04	163.89 ± 0.06	14.08 ± 0.04
27.15 ± 2.12	166.66 ± 0.06	14.40 ± 0.04	163.46 ± 0.06	14.13 ± 0.04
31.74 ± 2.47	166.43 ± 0.06	14.28 ± 0.04	163.13 ± 0.06	13.99 ± 0.04
37.11 ± 2.89	166.40 ± 0.06	14.38 ± 0.04	162.97 ± 0.06	14.09 ± 0.04

relative probability of various multi-chance fission reactions and so varies continuously across incident neutron energies.

Neutron emission also occurs immediately after scission from the fission fragments, thereby reducing their masses. There is a dearth of experimental data for this parameter for many isotopes including  $^{233}\text{U}$  and  $^{232}\text{Th}$ , so this value was found by using the General Description of Fission Observables (GEF) model version 2018/1.1 [12]. Each iteration of the  $2E$  analysis results in a new estimate for the mass of the fission fragment and therefore the neutron emission, which is mass dependent, and must be determined for each iteration, so it was run beforehand over the full range of incident neutron energies and a surface plot was interpolated across all masses and energies shown in Fig. 3. Then, when the iterative analysis was performed, it referenced this neutron-emission surface, thereby allowing the GEF code to be run with large enhancement factors for improved counting statistics.

#### IV. RESULTS

The average TKE was evaluated as the mean of a normal distribution of TKE values from individual fission events within a neutron energy bin. Neutron energy bins were set to increase in width logarithmically with increasing  $E_n$  to maintain counting statistics as neutron flux drops off at higher energy. The average TKE results for  $^{232}\text{Th}$  are shown in Fig. 4 along with other past experimental results with which the results of this work are in good agreement. The horizontal error bars represent the neutron-energy bins.

For many actinides, it is typical for average TKE to decrease with increasing  $E_n$  across the range shown in Fig. 4(a), however,  $^{232}\text{Th}$  is atypical in that the average TKE initially increases for  $E_n$  up to 5 MeV as observed by all but one of the past experimental results [9,11,13–16]. This trend of initially-rising average TKE has been observed in only one other actinide,  $^{238}\text{U}$ , and then only up to 1.5 MeV [18].

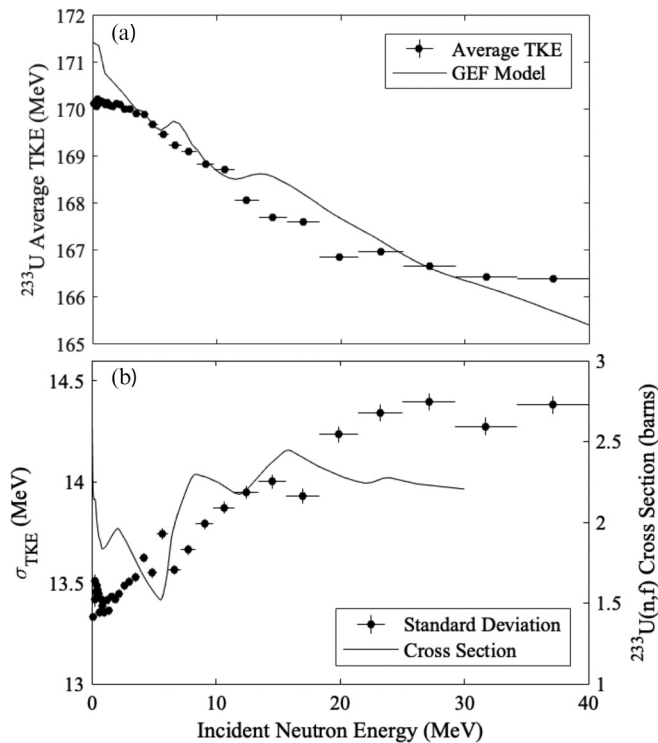


FIG. 5. (a) Average TKE in  $^{233}\text{U}(n, f)$  prior to neutron emission with the predicted value from the GEF model. (b) Standard deviation in TKE and the neutron-induced fission cross section for  $^{233}\text{U}(n, f)$ . Prompt neutron emission prior to scission is determined by using the multi-chance fission cross sections, as discussed in Sec. III C. Vertical error bars show statistical uncertainty; horizontal error bars correspond to neutron energy bins.

Importantly, the results from this work confirm this distinct trend for  $^{232}\text{Th}$  as well as provide validation of the method used. A comparison at higher neutron energy, as shown in Fig. 4(b), shows that the rising trend in average TKE at lower energy is arrested at approximately 6 MeV. This corresponds with the onset of second-chance fission, and the TKE undergoes a downward correction before stabilizing into a steady downward trend similar to that observed in other actinides [10,18–21].

The results for average TKE and the standard deviation in TKE for  $^{233}\text{U}$  pre-neutron emission are shown with the predicted TKE from the GEF and the neutron-induced fission cross section in Fig. 5. The results show a trend of steadily decreasing average TKE with increasing  $E_n$ . This general trend and rate of change are similar to those observed in other actinides such as  $^{238}\text{U}$  and  $^{239}\text{Pu}$  and are in generally good agreement with the model, even at high  $E_n$  [18,19]. However, the model predicts certain features, such as a prominent bump at 7 MeV and another at 14 MeV, that are not present in these results. Furthermore, the model predicts a higher average TKE at thermal  $E_n$  than shown in these results or than is reported by other past experimental results for this reaction [10]. Average TKE and standard deviation both before and after neutron emission for all incident neutron energies measured are tabulated in Table I.

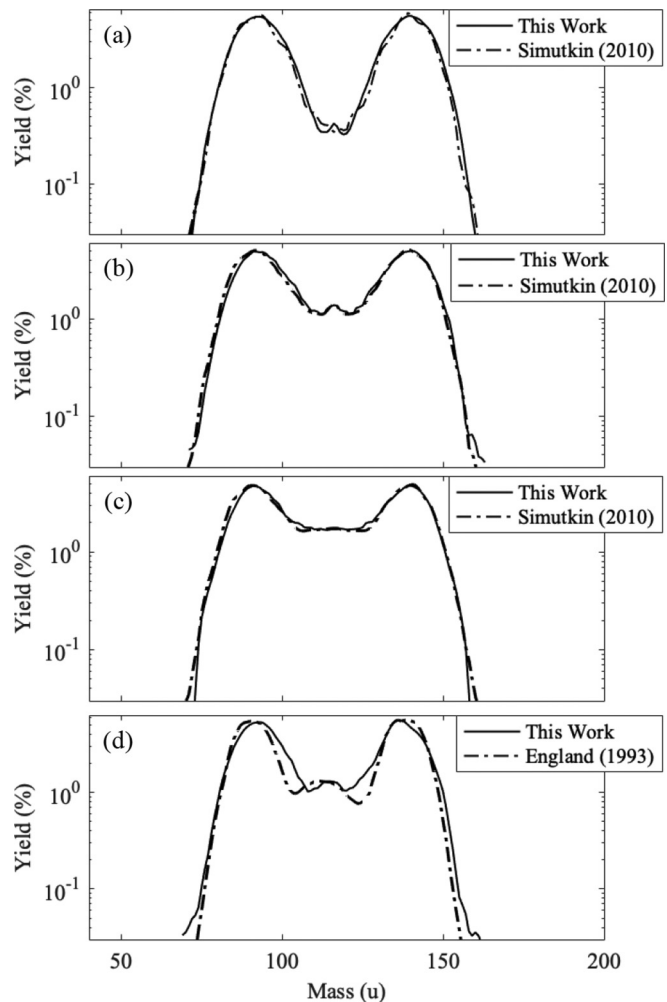


FIG. 6. Fission fragment mass yields for  $^{232}\text{Th}(n, f)$  shown at 5 amu resolution compared with Refs. [22,23] for neutron energies (a) 9–11 MeV, (b) 16–18 MeV, (c) 24–26 MeV, and compared with Ref. [20] for neutron energies (d) 13–15 MeV.

The mass resolution of a twin ionization chamber is 4–5 amu, which is not precise enough to distinguish fine features in the mass yield curves. Rather, these results are most useful for observing the shape of the mass yields and the trend with increasing  $E_n$ . The fission fragment mass yields for both  $^{232}\text{Th}$  and  $^{233}\text{U}$  exhibit a bimodal distribution at low energy with an increasing prevalence of symmetric fission with increasing  $E_n$ . The mass yield results for  $^{232}\text{Th}$  show strong agreement with past results at various incident neutron energy ranges, as shown in Fig. 6. These results confirm a distinct symmetric fission feature in the center of the curve at high  $E_n$ , as observed in other studies, which provides validation of the method used in this work.

The mass yield curves for  $^{233}\text{U}$ , shown in Fig. 7, exhibit the same characteristic bimodal distribution at low energy as observed in  $^{232}\text{Th}$  as well as many other actinides. As  $E_n$  increases, the two peaks become decreasingly distinct. Furthermore, the mass yield for  $^{233}\text{U}$  at thermal energy appears to be in good agreement with past results, as shown in Fig. 8 [24,25].

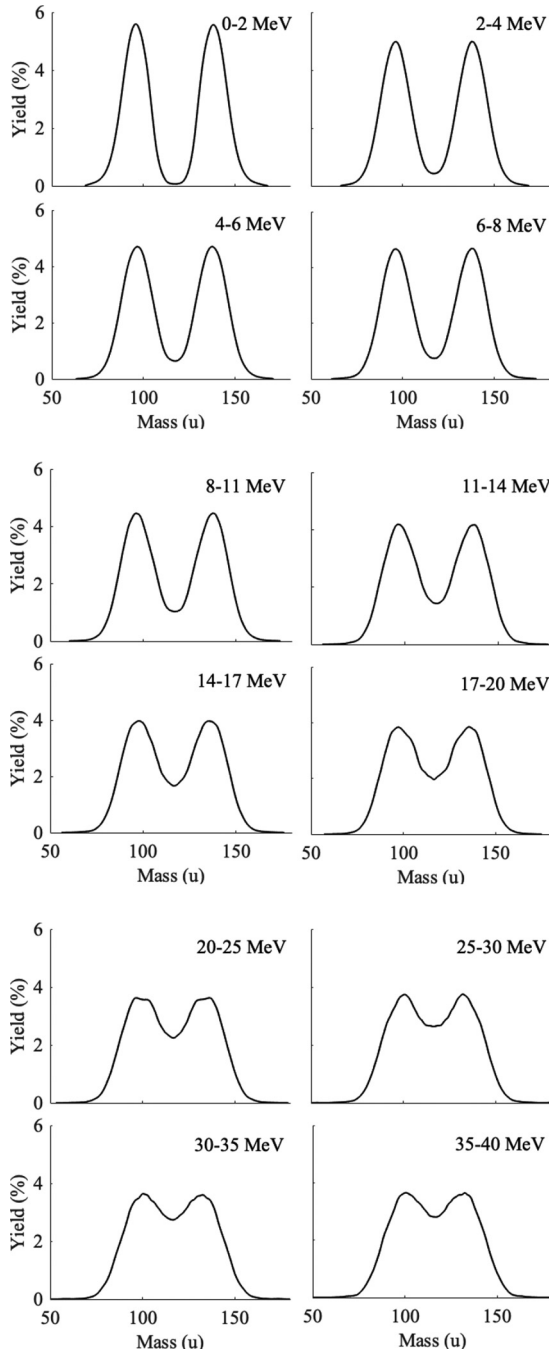


FIG. 7. Fragment mass yield curves for various  $E_n$  bins for  $^{233}\text{U}$ . Yield is normalized to 200% and shown at 5 amu resolution.

Fragment masses were compared to the TKE to characterize how this relationship changes with  $E_n$  to understand how the distribution of kinetic energy into different fragments drives the net change in average TKE, shown in Fig. 9. These plots show the distinctive bimodal mass distribution at low energy while symmetric fission is observed to fill in the center of the plot as  $E_n$  increases. These plots reveal how fragments from symmetric fission are on average correlated with lower TKE. As  $E_n$  increases, the prevalence of symmetric

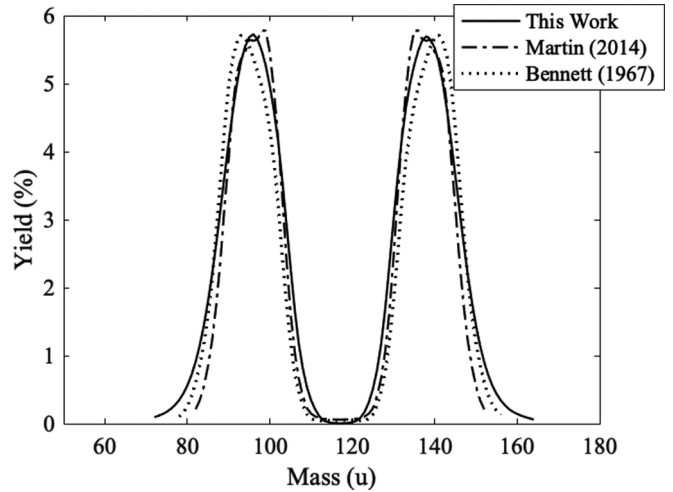


FIG. 8.  $^{233}\text{U}$  fission fragment mass distribution results comparison shown with 5 amu resolution at thermal neutron energy for pre-neutron emission [24,25]. Neutron emission is determined as discussed in Sec. III C using the GEF model.

fission increases, which drives the overall decrease in average TKE.

This experiment was a shape measurement of the average TKE, with the energy scale for the fragment set by previous measurements calibrated against thermal neutron-induced fission of  $^{235}\text{U}$ . The final uncertainties of the energy come from the uncertainties in the energy calibration fit parameters which incorporate uncertainties from the pulse height defect. Furthermore, the correction for prompt neutron emission contributes to systematic uncertainty since it is estimated based on the results of the GEF model.

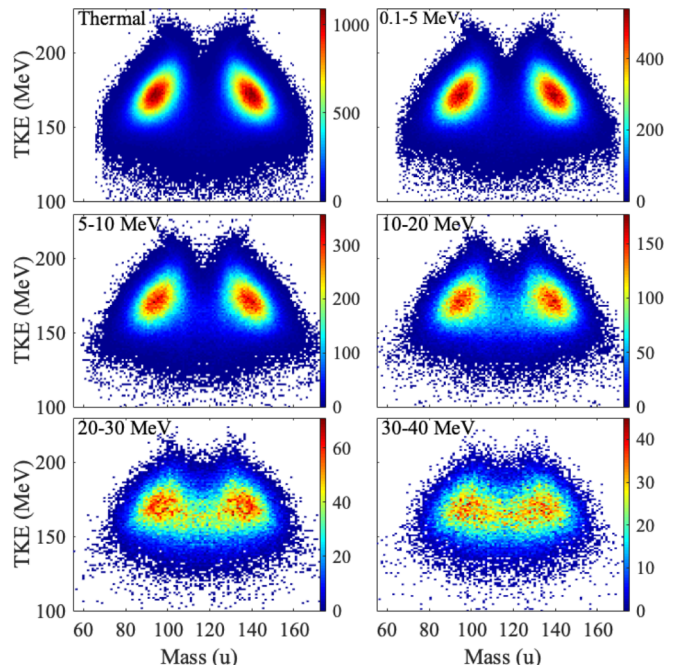


FIG. 9.  $^{233}\text{U}(n, f)$  fragment mass TKE distributions.

## V. CONCLUSION

The detector used in this experiment had high efficiency which made it possible to measure average TKE and mass yields over a wide range of energies and observe changes in trends of these values relative to  $E_n$ . This work extended measurements of these fission parameters to higher neutron energies than previously recorded and incorporated a novel approach to account for prompt neutron emission. By comparing the TKE to fragment masses at different  $E_n$ , it was shown that symmetric fission events were associated with lower average TKE. The increasing prevalence of symmetric fission at higher  $E_n$  was the driver of the overall decrease in average TKE. Since these data are slightly different from the model predictions, they will serve to improve future reactor design calculations by improving the input nuclear data and they provide a better understanding of fission in isotopes central to the thorium fuel cycle.

Further experiments should be performed to obtain measurements of neutron multiplicity for both isotopes to form a more accurate picture of the fission process in these isotopes. Future work is planned to measure TKE in additional isotopes, including  $^{237}\text{Np}$ , as well as experiments to obtain higher resolution in the mass yield curves to better identify dominant fission products.

## ACKNOWLEDGMENTS

This work benefited from the use of the LANSCE accelerator facility and was performed under the auspices of the US Department of Energy by Los Alamos National Security, LLC under Contract No. DE-AC52-06NA25396. University collaborators acknowledge support for this work from the U.S. Department of Energy Nuclear Energy Research Initiative Project No. 08-014 and the DOE-NNSA Stewardship Science Academic Alliances Program under Award No. DE-NA0002921.

- 
- [1] D. G. Madland, *Nucl. Phys. A* **772**, 113 (2006).
- [2] C. Budtz-Jørgensen, H.-H. Knitter, Ch. Straede, F.-J. Hamsch, and R. Vogt, *Nucl. Instrum. Methods A* **258**, 209 (1987).
- [3] P. W. Lisowski and K. F. Shoenberg, *Nucl. Instrum. Methods Phys. Res., Sect A* **562**, 910 (2006).
- [4] S. Mosby, F. Tovesson, A. Couture, D. Duke, V. Kleinrath, R. Meharchand, K. Meierbachtol, J. M. O'Donnell, B. Perdue, D. Richman, and D. Shields, *Nucl. Instrum. Methods A* **757**, 75 (2014).
- [5] D. Higgins, Ph.D. thesis, The Colorado School of Mines, 2018.
- [6] W. Loveland, *J. Radioanal. Nucl. Chem.* **307**, 1591 (2016).
- [7] M. B. Chadwick, M. Herman, P. Obložinský, M. E. Dunn, Y. Danon, A. C. Kahler, D. L. Smith, B. Pritychenko, G. Arbanas, R. Arcilla, R. Brewer, D. A. Brown, R. Capote, A. D. Carlson, Y. S. Cho, H. Derrien, K. Guber, G. M. Hale, S. Hoblit, S. Holloway, T. D. Johnson, T. Kawano, B. C. Kiedrowski, H. Kim, S. Kunieda, N. M. Larson, L. Leal, J. P. Lestone, R. C. Little, E. A. McCutchan, R. E. MacFarlane, M. MacInnes, C. M. Mattoon, R. D. McKnight, S. F. Mughabghab, G. P. A. Nobre, G. Palmiotti, A. Palumbo, M. T. Pigni, V. G. Pronyaev, R. O. Sayer, A. A. Sonzogni, N. C. Summers, P. Talou, I. J. Thompson, A. Trkov, R. L. Vogt, S. C. van der Marck, A. Wallner, M. C. White, D. Wiarda, and P. G. Young, *Nucl. Data Sheets* **112**, 2887 (2011).
- [8] L. Meitner and O. Frisch, *Nature (London)* **143**, 239 (1939).
- [9] T. Trochon, H. Abou Yehia, F. Brisard, and Y. Pranal, *Nucl. Phys. A* **318**, 63 (1979).
- [10] C. Wagemans, *The Nuclear Fission Process* (CRC Press, Boca Raton, FL, 1991).
- [11] S. T. Lam, L. L. Yu, H. W. Fielding, W. K. Dawson, and G. C. Neilson, *Phys. Rev. C* **28**, 1212 (1983).
- [12] K. Schmidt, B. Jurado, and C. Amouroux, Nuclear Energy Agency, Organization for Economic Cooperation and Development, GEF code version 2018/1.1 (2018).
- [13] J. Kiesewetter, K. Brinkmann, F. Baumann, H. Freiesleben, and H. Sohlbach, *Nucl. Phys. A* **540**, 75 (1992).
- [14] W. Holubarsch, E. Pfeiffer, and F. Gönnewein, *Nucl. Phys. A* **171**, 631 (1971).
- [15] A. Sergachev, *Sov. J. Nucl. Phys.* **17**, 362 (1968).
- [16] N. Dyachenko, B. Kuzminov, I. Kuks, Y. Nemilov, B. Nikolaev, Y. Selitskii, A. Sergachev, and V. Funshtein, *Sov. J. Nucl. Phys.* **28**, 8 (1976).
- [17] J. King, R. Yanez, W. Loveland, J. S. Barrett, B. Oscar, N. Fotiades, F. Tovesson, and H. Y. Lee, *Eur. Phys. J. A* **53**, 238 (2017).
- [18] F. Tovesson, D. Duke, V. Geppert-Kleinrath, B. Manning, D. Mayorov, S. Mosby, and K. Schmitt, *EPJ Web Conf.* **169**, 00024 (2018).
- [19] K. Meierbachtol, F. Tovesson, D. L. Duke, V. Geppert-Kleinrath, B. Manning, R. Meharchand, S. Mosby, and D. Shields, *Phys. Rev. C* **94**, 034611 (2016).
- [20] T. R. England and B. F. Rider, ENDF-349: Evaluation and Compilation of Fission Product Yields (Tech. rep.), Los Alamos National Laboratory (1994).
- [21] F. Vivès, Ph.D. thesis, L'Université de Bordeaux, 1998.
- [22] V. D. Simutkin, Ph.D. thesis, Uppsala Universitet, 2010.
- [23] V. D. Simutkin, S. Pomp, J. Blomgren, M. Österland, R. Bevilacqua, P. Andersson, I. V. Ryzhov, G. A. Tutin, S. G. Yavshits, L. A. Vaishnena, M. S. Oegin, J. P. Meulders, and R. Prieels, *Nucl. Data Sheets* **119**, 331 (2014).
- [24] M. Bennett and W. Stein, *Phys. Rev.* **156**, 1277 (1967).
- [25] F. Martin, C. Sage, G. Kessedjian, O. Sérot, C. Amouroux, C. Bacri, A. Bidaud, A. Billebaud, N. Capellan, S. Chabod, X. Doligez, H. Faust, U. Köster, A. Letourneau, T. Materna, L. Mathieu, O. Méplan, and S. Panebianco, *Nucl. Data Sheets* **119**, 328 (2014).